

RSC Advances



This is an *Accepted Manuscript*, which has been through the Royal Society of Chemistry peer review process and has been accepted for publication.

Accepted Manuscripts are published online shortly after acceptance, before technical editing, formatting and proof reading. Using this free service, authors can make their results available to the community, in citable form, before we publish the edited article. This *Accepted Manuscript* will be replaced by the edited, formatted and paginated article as soon as this is available.

You can find more information about *Accepted Manuscripts* in the [Information for Authors](#).

Please note that technical editing may introduce minor changes to the text and/or graphics, which may alter content. The journal's standard [Terms & Conditions](#) and the [Ethical guidelines](#) still apply. In no event shall the Royal Society of Chemistry be held responsible for any errors or omissions in this *Accepted Manuscript* or any consequences arising from the use of any information it contains.

ARTICLE

Laser-induced transformation of freestanding carbon nanotubes into graphene nanoribbons

Hai Hoang Van,^{ab} Kaelyn Badura,^b and Mei Zhang^{ab}

Graphene nanoribbons (GNRs) were successfully produced by using a laser to transform the tubular structure of multiwalled carbon nanotubes (CNTs). A laser beam was controlled to scan along the longitudinal axis of the freestanding aligned CNT sheets in air. As a result of the thermal interactions between the laser beam and CNTs, local oxidation was observed to happen at the graphitic walls of CNTs. This oxidative phenomenon was assisted by the laser-induced thermal expansion of the graphitic tube which transformed the tubular structure of CNTs. The direction of the laser irradiation led to the production of two-dimensional graphene nanoribbons. The produced GNRs were freestanding and featured smooth surfaces. This laser scanning method was simple and industrially scalable to continuously produce GNRs.

1. Introduction

Graphene is an allotrope of carbon (C) with a two-dimensional (2D) monoatomic-thickness, exhibiting superior mechanical, thermal, and electrical properties.^{1–3} Specifically, graphene is a semimetal with a zero bandgap.⁴ This zero bandgap is widened by patterning graphene into graphene nanoribbon (GNR),⁴ whose width is principally smaller than 50 nm. GNRs with widths lower than 10 nm become semiconductors regardless of the geometry of their edges.^{5,6} Li *et al.* produced GNRs with width less than 10 nm which had bandgaps opened up to 400 meV.⁶ Field-effect transistors using these GNRs achieved a $I_{\text{ON}}/I_{\text{OFF}}$ ratio of over 10^6 .⁶ The existence of tunable electronic characteristics have made GNRs an outstanding candidate for pushing the traditional physical limit of the materials in contemporary transistor technology. GNRs also exhibited broadband saturable absorption in both the optical and microwave bands, opening applications in optical and microwave communication.⁷ Additionally, GNRs are capable of performing broadband polarizing effect in the visible to near-infrared wavelengths, presenting a modulation solution for optical-fiber ultra-broadband communication.⁸ Moreover, due to its high surface area and its outstanding thermal, electrical, and electronic properties, GNRs can be used as the active materials in various applications including biosensors,⁹ chemical sensors,^{10,11} electronic memory devices, processing devices,^{12,13} nano-electromechanical systems,¹⁴ and composites.¹⁵

Several approaches have been used to obtain GNRs. Lithographic patterning on graphene sheets and chemical vapor deposition (CVD) were used to create GNRs with widths greater than 20 nm.^{16,17} Unzipping carbon nanotubes

(CNTs) is another promising way to produce GNRs.^{5,18,19} There have been many methods proposed to unzip CNTs, which can be classified into chemical-scissor unzipping methods and non-chemical based unzipping methods.

In the chemical-scissor unzipping methods, the unzipping processes were based on the oxidation between chemical compounds (or catalysts) and CNTs, which resulted in the longitudinal cutting of the graphitic shells. Kosynkin *et al.* utilized concentrated sulfuric acid H_2SO_4 and potassium permanganate (KMnO_4) to oxidize the CNTs, leading to the opening of the existing carbon-carbon double bonds.²⁰ To avoid the severe oxidation of CNTs caused by H_2SO_4 and KMnO_4 , Elias *et al.* utilized metal nanoparticles (Ni and Co) to cut the C-C bonds.²¹ The method Elias *et al.* used was based on the catalytic hydrogenation of CNTs caused by those nanoparticles. However, the unzipping direction was affected by the defect levels and the chirality of the CNT walls. Due to the arbitrary nature of these characteristics, the unzipping direction was random. The chemical compounds used in unzipping processes affected the properties of GNRs and increased the complexity of the process. For example, the oxidation process using H_2SO_4 and KMnO_4 did not only unzip the CNTs but it also formed the carboxyl and hydroxyl functionalities along the GNRs edges. Consequently, an additional reduction process was required to remove these functional groups. However, the electronic properties of the reduced GNRs were not comparable to the properties of the GNRs directly patterned from graphene sheets.²¹

In the non-chemical based unzipping methods, the tubular structure was not unzipped by using a chemical reaction. Instead, external influences such as plasma bombardment,^{18,22,23} electric current-induced heating,²⁴ thermal stress,^{25,26} or mechanical impart²⁷ were used to cause

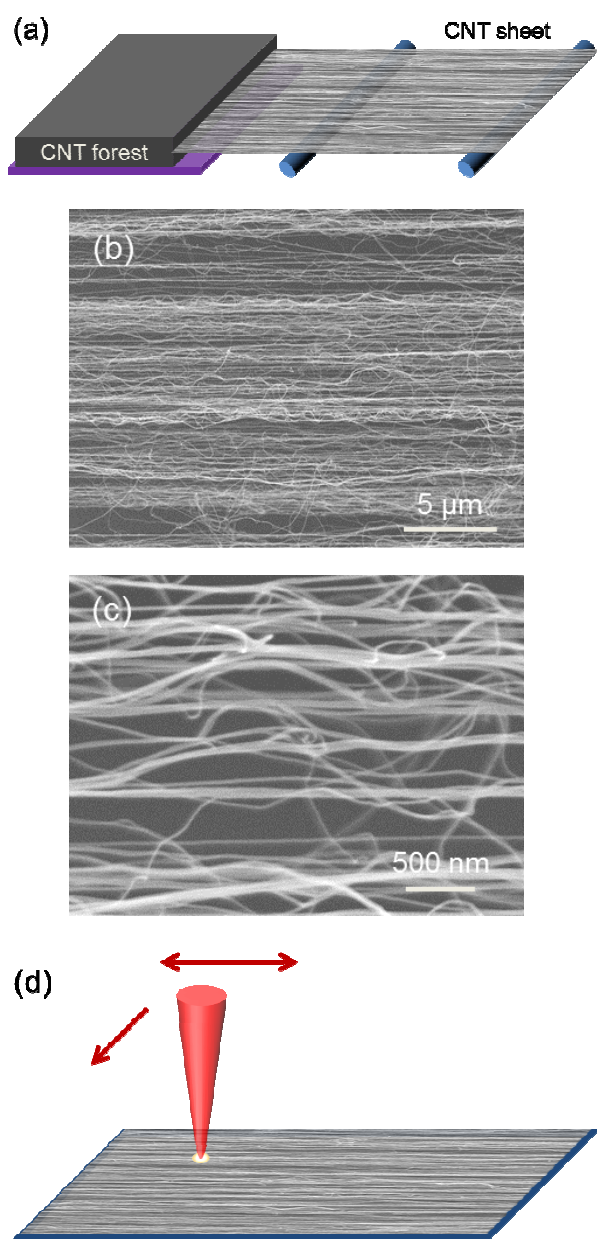


Fig. 1 (a) Schematic illustration of the CNT sheet production process. The CNT sheet was produced by laterally drawing CNTs from the edge of CNT forest; (b) and (c) SEM images of the freestanding CNT sheet, respectively; (d) Applying CNT sheet on metal frame and raster-scanning the CNT sheet surface by the continuous IR laser beam.

the structural transformation of CNTs. Chemical agents, such as acids, were used to introduce structural defects to graphitic walls of CNTs;^{25,26} thus the CNT structure became more likely to be transformed. The abrupt thermal-stress methods were normally performed with the assistance of this defect-generation technique to easily breakdown the tubular structure. However, due to the random distribution of the defects on the graphitic walls and the uncontrollable chirality of the CNTs, the breakdown direction of the tubes was random. As a result, many CNTs were fragmented.^{25,26}

Similar to the chemical-scissor unzipping methods, the usage of chemicals did not only contaminate CNTs but also created functional groups along the edges of the defective sites.

The current-induced heating methods demonstrated the concept of using extremely high temperature (around 3000°C) to unwrap CNT walls one by one without using any chemical. The produced GNRs exhibited a high quality graphitic structure. However, this method could only be applied to individual CNTs at a time. The mechanical impart method produced GNRs with the heavily damaged graphitic structures due to the extreme collision between CNTs and metal target at a high velocity. The plasma methods utilized ion bombardment to damage the CNT surface, gradually removing carbon atoms from CNT walls. Finally, GNRs were produced when about half of the tubes were removed. The structural quality of the produced GNRs need to be carefully investigated because during the bombardment process, the generated ions can also attack the opened CNTs, consequently damaging the produced GNRs.

In this paper, we report a solid-state method for the transformation of the tubular structure of CNTs into the 2D structure of GNRs, addressing those issues relating to the contamination and the structural quality of the produced GNRs. Freestanding aligned CNT sheets were used as the starting material. A continuous infrared laser was controlled to scan along the CNT sheet alignment. The thermal effect induced by the laser irradiation, including thermal oxidation of the graphitic walls and thermal expansion of the tubes opened the CNT structure. The residual pieces of graphene on the surface of the produced GNRs were removed by further applying laser scanning with lower irradiation power, resulting in smooth surfaced GNRs. The produced GNRs typically had width distributions from 10 nm to 15 nm, making them suitable for electronic applications.²⁸

2. Experimental

The freestanding CNT sheet was produced by laterally drawing CNTs from a CNT forest [Fig. 1(a)].²⁹ The CNTs in the sheet were well-aligned in the drawing direction (Fig. 1(b)) and they were multiwalled CNTs with 4-8 walls, 7-10 nm in diameter, and around 450 μm in length. The average thickness of the CNT sheet was approximately 18-20 μm.³⁰ The small CNT bundles and the individual CNTs formed an interconnected freestanding sheet [Fig. 1(c)]. A single-layer CNT sheet was applied onto a metal frame. A continuous CO₂ laser (VLS2.30, Universal Laser Systems Inc.) with an infrared (IR) wavelength of 10.6 μm was utilized to raster-scan the entire sheet surface [Fig. 1(d)]. The laser beam diameter on the focal plane was 100 μm. The CNT sheet was positioned at the focal distance of the laser beam to acquire the highest energy density. The laser irradiation energy was proportional to the laser output power and inversely proportional to the scanning speed. The effect of the laser power on the transformation of CNTs was investigated. In this experiment, the laser output power was controlled to change from 0 to 100 mW and the scan speed was kept at 20 cm/s. The thermal stability of CNTs was studied by using thermogravimetric analysis (TGA Q50, TA Instruments). The energy absorption of CNT sheet at 10.6 μm wavelength was determined by Fourier transform infrared spectroscopy (FTIR, Nexus 470 FTIR E,S,PTM, Thermo Nicolet). Raman spectra were obtained using a micro-Raman system (Renishaw, Inc., InVia Raman). The Raman spectrometer

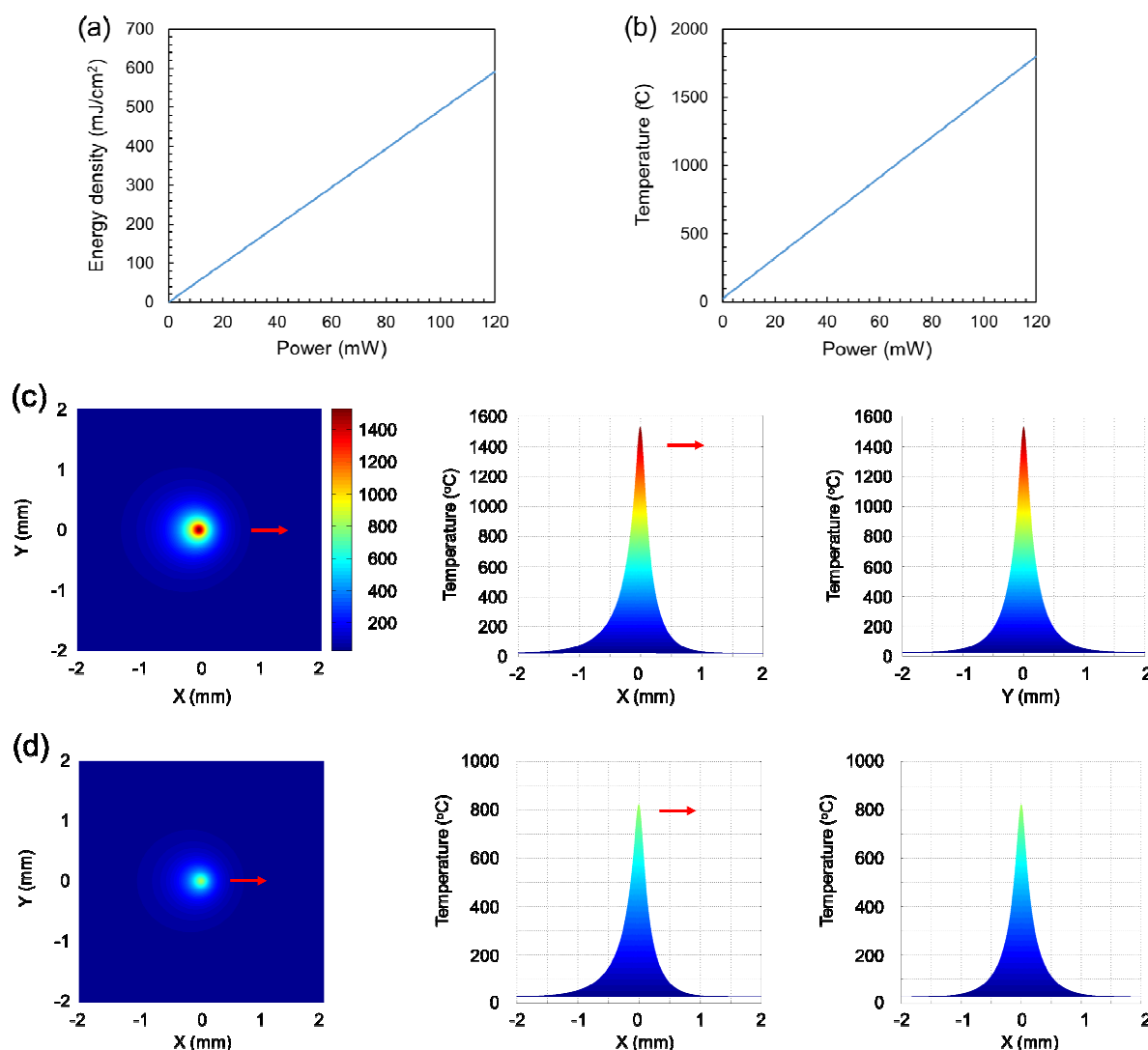


Fig. 2 (a-b) Energy density irradiating on CNT sheet and the corresponding temperature increase (respectively) when the laser power changed from 0 mW to 120 mW at the scanning speed of 20 cm/s; (c) and (d) Temperature distributions on the CNT sheet when laser beam irradiates the CNT sheet with the output power of 100 mW and 55 mW, respectively. The scanning speed was 20 cm/s. The arrows indicate the direction of laser beam movement.

was calibrated using a standard silicon substrate. A laser with wavelength of 785 nm and beam size of 10 μm was used to excite the Raman scattering. The scanning electron microscope (SEM FE 7407F, JEOL Ltd.) was used to observe the structure of CNT sheet drawn from CNT forest. The transmission electron microscope (TEM JEM-ARM200cF, JEOL Ltd.) with Electron energy loss spectroscopy (EELS Gatan Inc.) was utilized to analyze the structural transformation and the chemical characteristics of CNTs before and after laser irradiation.

3. Results and discussion

3.1 Interaction between laser irradiation and CNT sheet

When the CO_2 laser beam perpendicularly irradiated the CNT sheet, a portion of its energy was reflected from the surface of CNTs due to the difference in the refractive indices.³¹ The remaining energy kept traversing into the sheet. The

traversing beam was scattered inside the sheet due to the porous structure and the high surface area. The rest of laser energy was transmitted through the structure. The amount of energy absorbed by CNT sheet was measured by FTIR.

When the CNTs were struck by photons from the incident laser beam, the carbon atoms became more mobile, vibrating much stronger. The lattice structure conducted the vibration to neighboring atoms; consequently the irradiated area was heated. The energy absorption and the vibration of the interacting atoms depended on the wavelength and the phase of the incident light wave. Different from other regular light sources such as sun, light bulb, or light-emission diode, a laser wave is monochromatic and coherent, meaning that the beam is transmitted with a single wavelength as well as spatially and temporally in phase. As a result, the thermal response from CNTs was much stronger due to the uniform energy absorption and the resonant interaction between the incident light wave and the vibrating carbon atoms. In

addition, the laser energy was concentrated in the small beam, consequently intensifying the thermal effect.

During the laser irradiation process, intense white light was observed as being emitted from the irradiated area. This light emission was the incandescence induced when the target was heated to a high temperature.³² The laser power and the irradiation time, related to the scanning speed of the moving laser, determined how high of a temperature the CNTs could reach. When the laser power increased and the irradiation time increased, more irradiation energy was delivered to the samples, further increasing the temperature of CNTs.

The heating area moved along the sheet alignment following the laser scanning direction. Thermal transport was described as the heat flow between the graphitic walls within the same CNTs and the flow from one CNT to other CNTs via tube-tube interface.³³ The flow direction was dependent on the thermal conduction direction of CNTs and the movement direction of heat source.³³

The temperature distribution induced from the laser linearly scanning on a thin CNT sheet was estimated by applying a 2D thermal simulation model which was introduced by Brockman *et al.*³⁴ The heat conductivity equation used to calculate the temperature when the direction is along the x-axis is described as:

$$\rho C_p u \frac{\partial T}{\partial x} = \kappa \left(\frac{\partial^2 T}{\partial x^2} + \frac{\partial^2 T}{\partial y^2} + \frac{\partial^2 T}{\partial z^2} \right) T \quad (1)$$

where the structure and the thermal properties of the CNT films are characterized by ρ as density (kg/m^3), C_p as specific heat capacity (J/kgK), and κ as thermal conductivity (W/mK). The heat transfer coefficient α ($\text{W/m}^2\text{K}$) (relating to the surface area of the structure) is included in the boundary conditions at the top and the bottom CNT film surfaces by considering the heat loss due to the thermal convection to environment. The effect of laser scanning is considered with the scanning velocity u (m/s) and the heat flux q , which is integrated as the boundary condition for the heat conductivity equation (1).

The 2-dimensional temperature distribution is computed as:³⁴

$$T = \theta T_* + T_g \quad (2)$$

where T_g is ambient gas temperature (K) and T_* and θ are described by the following equations:

$$\begin{aligned} T_* &= \frac{q_0}{h} = \frac{4\sigma r_b^2}{h} \\ \theta &= \frac{\sqrt{2\pi}}{1 + \sqrt{1 + F}} \exp(Bi + 2Pe(x + Pe) - \sqrt{F}) \\ F &= 4(Bi + Pe^2)[y^2 + (x + Pe)^2] \\ Pe &= \frac{\rho C_p u r_b}{\kappa} \\ Bi &= \frac{\alpha r_b}{\kappa} \end{aligned}$$

where q_0 is the maximum laser heat flux density (W/m^2), r_b is the effective laser beam radius (m), and h is the film thickness (m).

It was noticed by Brockman that this 2D model was valid when the beam size was greater than the sheet thickness and when the sheet thermal conductivity was large.³⁴ CNTs have been proven to have high thermal conductivity.³⁵ Therefore, the Brockman model was suitable to calculate the temperature generated by laser-CNT sheet interaction.

Aliev *et al.* measured the thermal properties of single-layer freestanding aligned CNT sheet.³⁶ The thermal conductivity along sheet alignment was 50 W/mK . This experimental conductivity of CNT sheet was much lower than the CNTs' intrinsic thermal conductivity, 3000 W/mK for multiwalled CNTs³⁷ and 3500 W/mK single-walled CNTs.³⁵ The thermal conductivity decrease was explained by

the dangling interface between the bundles, the phonon scattering within the bundles, and the defects in the individual CNTs.³⁶ In addition, the specific heat capacity was 700 J/kgK , regardless of the sheet length. The heat transfer coefficient for single-layer CNT sheet was $35 \text{ W/(m}^2\text{K)}$.³⁸ FTIR was utilized to measure the energy absorption of CNT sheets at a laser wavelength of $10.6 \mu\text{m}$. The FTIR spectra showed that CNT sheets absorbed 18% of irradiating energy from the IR laser beam (Fig. S1 in Supporting Information).

Fig. 2(a) shows the energy density generated by laser beam of output power of up to 120 mW scanning freestanding ultrathin CNT sheet at a speed of 20 cm/s . The computed temperature induced by the corresponding laser irradiation conditions is presented in Fig. 2(b). At the same irradiation time, temperature increased monotonically with the power increase. Matlab program was used to calculate the temperature distribution on the surface of a CNT sheet irradiated by a moving laser beam. Equation (2) was applied for the calculation. Fig. 2(c) demonstrates the temperature result when the CNT sheet was scanned by a laser beam with output power of 100 mW at the scanning speed of 20 cm/s . The temperature was possibly increased up to 1523°C . The arrow in the figure indicated the scanning direction of the beam. The energy absorption level was 17% after the first scan (Fig. S1 in Supporting Information). The CNT sheet was further irradiated with the laser power of 55 mW . Simulation results estimated that the sheet temperature increased up to 821°C [Fig. 2(d)]. Along the scanning path (x-axis), temperature had a tailed-distribution. This tailed-distribution resulted from a cooling effect of the irradiated sheet and the movement of the laser beam. The tail length became shorter when the thermal conductivity of the sheet increased and the scanning speed of laser was faster. Temperature was distributed symmetrically to both sides of the scanning direction.

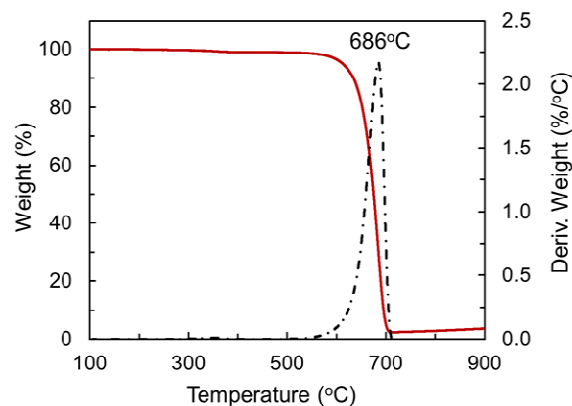


Fig. 3 TGA spectrum for CNT in air environment.

The laser scanning experiments were performed in the ambient environment with air, resulting in the oxidation of CNTs at high temperatures. TGA was employed to study the thermal stability of CNTs. Air was used for the analysis with a flow of 60 mL/min . The temperature was increased at the rate of 10°C/min . The results showed that CNTs started to oxidize at around 550°C and reached the highest oxidation rate at 686°C [Fig. 3]. Therefore, under the extremely high temperature condition induced by laser-CNT sheet interaction, the CNT sheets should be oxidized.

3.2 Formation of GNRs

Laser beams are directional, i.e. photons transmit in the same direction with small divergence. The irradiating energy was confined in the narrow beam size, i.e. 100 μm , generating a large energy intensity. In addition, the laser beam is monochromatic and coherent, inducing the strong and uniform responses from the material. Consequently, the laser beam was capable of remarkably increasing the temperature with the strong gradient during the scanning of the CNT sheet. Due to the high surface area of CNT sheet and the high thermal conductivity of CNTs, and the existence of thermally affected area the consequent oxidized area was localized at the irradiated spot.

freestanding porous sheets [Fig. 2(b)]. In the experiments, CNT sheets were placed on the focal plane of the laser beam in order to allow the highest irradiation intensity to be delivered to the CNTs. When the laser power was increased or the irradiation time was increased, the laser intensity was increased accordingly. The different laser intensity led to difference in transformation of the tubular structure of CNTs. Fig. 4(b-e) demonstrates different structural transformations of CNTs after being scanned by a laser beam of 100 mW at a scanning speed of 20 cm/s. According to computations, the CNT sheet was irradiated by an energy density of 498 mJ/cm^2 and was consequently heated up to 1523°C [Fig.

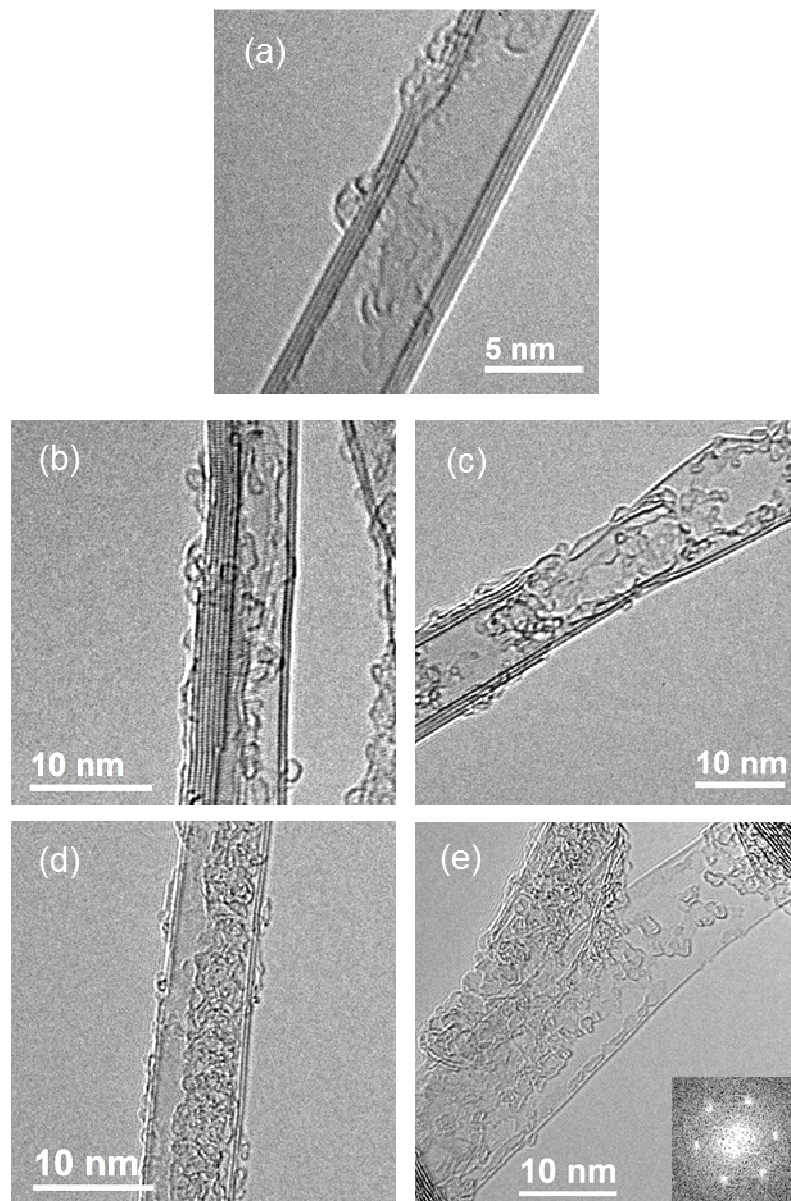


Fig. 4 TEM images displaying the structure of multiwalled CNTs before and after being scanned by the laser: (a) Typical original multiwalled CNT with four graphitic walls; (b) oxidized CNTs with one side of the tube showing double-walled structure and the other side containing seven graphitic walls; (c) oxidized CNT with half of its length unzipped and the other half oxidized; (d) DWCNTs with the oxidized graphitic walls remaining on the tube surface; (e) single-layer GNR with small residuals remaining from the outer CNT walls. The inset in (e) is Fast Fourier Transform pattern of the corresponding GNR image)

Original CNTs used for the experiments typically had 4 to 8 walls [Fig. 4(a)]. Those CNTs were directionally aligned in

2(b)]. Thus, the thermal oxidation was initiated at the defect sites on the tube surface.³⁹

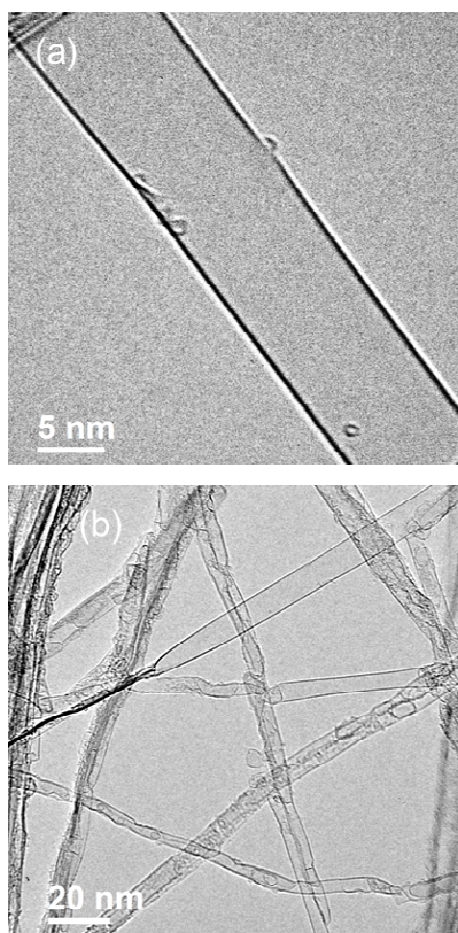


Fig. 5 TEM images of (a) individual GNR and (b) GNR array when the GNR surface was cleaned by laser irradiation with laser power of 55 mW and scanning speed of 20 cm/s.

After irradiating the surface, the laser beam traversed into the sheet, scattering within the sheet due to the high surface area of the porous structure.⁴⁰ The scattered beam was favorable in improving the interaction between the incident beam and the individual CNTs inside the sheet. Fig. 1(c) shows a CNT sheet with the bundled CNTs aligned along the sheet direction and the local isolated CNTs crossing between the bundles. These freestanding CNTs were approximately aligned along the scanning direction because the CNT diameter was much smaller than the beam diameter. The high surface area of those isolated CNTs highlighted the fast cooling of the heated areas. Furthermore, the oxidation at those areas was happening isotropically along the tubular circumferences.

On the contrary, under the same irradiation conditions, CNT bundles absorbed more energy than isolated CNTs due to the higher structural density of packed CNTs and the longer transmitting path through the bundles (Beer-Lambert law). Consequently the CNT bundle temperature was higher than the isolated CNT temperature, resulting in stronger oxidation at the bundle surface. The oxidation induced at the CNT bundles was anisotropic, relating to the non-uniform interface between the bundled CNTs and the oxygen. The oxidation happened more favorably at the CNTs surrounding the bundles which had direct interface with the oxygen in air in contrast with the inner CNTs that were isolated from the

environment. Accordingly, the transformed CNTs could have one longitudinal half oxidized with many walls removed and the other half with many walls retained. Fig. 4(b) demonstrates a modified CNT with one side showing double-walled structure, i.e. outside graphitic walls were oxidatively removed, and the other side having seven graphitic layers remaining. Due to the high flexibility, the entangled CNTs in bundles could appear with half of the length confined within the bundle and the other half freely exposed to oxygen. As a result, the dangling tube segment was opened and the other segment was partially oxidized with some graphitic walls removed [Fig. 4(c)].

Laser energy was scattered immensely inside the sheet due to the high structural porosity,⁴⁰ irradiating the inside-sheet CNTs at different angles. Consequently, these CNTs were also heated but not as strongly as the CNTs that were under direct irradiation. The thermal oxidation at those inside-sheet CNTs initially happened at the CNT defects, breaking the C-C bonds through the formation of carbonyl groups.^{19,41,42} In addition, CNTs radially and axially expanded under the high temperature.^{43,44} The oxidation-created vacancies which, when assisted by the thermal stress at high temperatures, fragmented the outside tubular walls and leaving graphitic residuals on the inner tube surface.⁴² Fig. 4(d) demonstrates double-walled CNT (DWCNT) with outer walls oxidized.

Fig. 4(e) shows a 13 nm-width single-layer GNR produced by unzipping a CNT, revealing how the GNR was produced. The inset is the corresponding Fast-Fourier Transform diffraction pattern, displaying a single hexagonal ring. This hexagonal pattern confirmed the graphitic and single-layered structure of the produced GNR.

The production of a GNR from a multiwalled CNT was the result of combined processes of spontaneous removal of the outer graphitic walls and the transformation of the innermost tube. The oxidation process happening on the CNT surface removed the outer walls. Due to the high curvature of smaller tubular diameters, the carbon atoms of the innermost tube were more active than the atoms on the outer walls.⁴⁵ Consequently, during the oxidative process happening at the outer walls, the oxidation also penetrated into the graphitic walls to oxidize the inner tubes. Some TEM images (not shown here) demonstrated that oxidation perforated the outer walls of DWCNTs to oxidize the innermost tubes. As the result, after the outer walls were removed, the thermal expansion stress and the curvature-induced stress widened the opened area of the innermost tube. As a result of the laser scanning along the CNT alignment, the laser-induced thermal stress directed the tube-opening direction along the tubular axis.⁴⁶ Additionally, the oxidation was more preferable to occur following the tube opening direction, where the stress was focused, instead of circumferentially cutting the graphitic layers.⁴¹ Therefore, GNRs were produced along the CNT axis [Fig. 4(e)]. The produced GNRs had some carbon-based domains remaining on the GNR surface as the residuals of the oxidized graphitic walls.

Raman spectra showed an increase in the intensity ratio of D-band to G-band (I_D/I_G) from 1.17 to 1.32 when the CNT sheet was irradiated by laser (Fig. S2 in Supporting Information). The I_D/I_G increase resulted from the graphitic defects in the edges of the produced GNRs, the features on the GNR surfaces, and the incomplete-opened CNTs (Fig. 4(b)-4(d)).

GNR surfaces were cleaned by using laser to further oxidize the small carbon domains attached to the GNR surface. Fig. 5(a) and 5(b) show the TEM images of both GNR and GNR array after laser post-treatment, respectively. Laser was used to scan the sample with a power of 55 mW and a scanning speed of 20 cm/s. The laser irradiation generated an energy density of 277 mJ/cm², increasing the CNT temperature up to 821°C (as calculated in Fig. 2(d)). Raman spectra of the GNRs before and after post-treatment process did not show any obvious difference (Fig. S3 in Supporting Information). The residuals from the previous step were very susceptible to the oxidation, thus being oxidized easily. The oxidation process also happened along the edges of the GNRs. However, calculations of the energy required to oxidize the carbon atoms showed that the oxidation was more likely to occur along the edges of a graphene layer as compared to penetrating inward into the graphene sheet.⁴¹ Consequently, the oxidation at GNRs mostly happened along the edges instead of cutting through the graphene sheet. Due to the size difference between the GNRs and the carbon domains, the oxidation occurring along GNR edges hardly changed the graphitic structure of the GNRs. Besides the oxidation happening along the GNR edges, laser irradiation also improved the graphitic structure of GNRs via the self-healing effect, occurring when carbon atoms reorganized their crystal structure due to high temperature exposure.

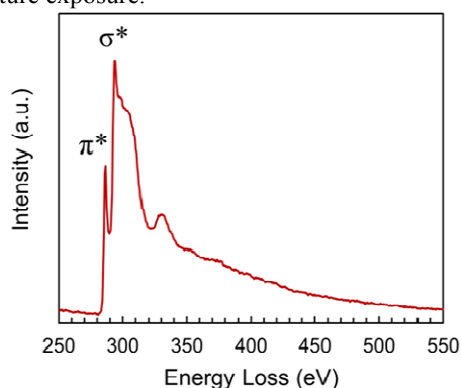


Fig. 6 EELS spectrum of overlapped GNRs.

EELS was utilized to analyze the chemical properties of GNRs at the atomic scale. Fig. 6 shows the EELS spectrum of the overlapped GNRs. The sharp peak π^* , at 286 eV, is due to the electron transition from 1s core level to the π^* band. Similarly, the other peak at σ^* , at 293 eV, is generated by the transition from 1s to σ^* band. These spectral peaks highlighted the K edge of the carbon atoms of CNTs and graphene.⁴⁷ These transitions may also feature the bonding between the carbon atoms and the oxygen atoms for the σ bond and the π bond. However, the oxygen K edge characterized by a peak at 530 eV⁴⁸ was not shown in the resultant EELS spectra, which may relate to the resolution limit of the equipment. Therefore, these π^* and σ^* peaks contained limited information about the oxygen-contained contaminants. This limited information can be explained due to the oxidation process occurring at high temperature of CNTs. The oxygen molecules in air oxidized the graphitic walls, generating CO₂ gas. Furthermore, the carbonyl group created on the GNR edges when oxygen molecules cut the carbon-carbon bonds can be thermally removed at 200°C,⁴⁹ which is lower than the oxidation point of CNTs. Therefore, the oxygen atoms were desorbed from the produced GNRs.

4. Conclusions

The GNR production process was performed by scanning a continuous laser beam along the alignment of freestanding CNT sheets in air. The produced GNRs were attributed to the local laser-induced oxidation which occurred at the graphitic walls, the thermal expansion of the tubular structure at high temperature, and the movement direction of the laser beam. The reported method exhibited advantages in producing GNRs. First of all, the starting material, the freestanding aligned CNT sheets, can be effectively and efficiently fabricated. The laser can quickly scan along the CNT alignment and simultaneously produce many GNRs. This method does not utilize aqueous solutions such as H₂SO₄ and KMnO₄ to open the nanotube. Therefore the contamination is limited and the subsequent purification process is unnecessary. The graphitic residuals on the GNR surface can be easily removed by further applying laser scanning with lower power and high scanning speed. Finally, GNRs were produced as freestanding; therefore GNR utilization does not require a transfer process from the synthesis substrate (as produced by other methods) to device substrates. The high quality GNRs are promising as an excellent candidate for electronic devices and sensors.

Acknowledgements

This work was supported by GP fund from Florida State University (FSU). The GNR observation was carried out at the FSU TEM facility, funded by the FSU Research Foundation, and supported by the NHMFL with NSF DMR-0654118 and the State of Florida.

Notes and references

^a Industrial and Manufacturing Engineering Department, FAMU-FSU College of Engineering, 2525 Pottsdamer Street, Tallahassee, Florida 32310-6046

^b High-Performance Materials Institute, Florida State University, 2005 Levy Ave., Tallahassee, Florida 32310

- C. Lee, X. Wei, J. W. Kysar and J. Hone, *Science*, 2008, **321**, 385–8.
- K. I. Bolotin, K. J. Sikes, Z. Jiang, M. Klima, G. Fudenberg, J. Hone, P. Kim and H. L. Stormer, *Solid State Commun.*, 2008, **146**, 351–355.
- A. A. Balandin, S. Ghosh, W. Bao, I. Calizo, D. Teweldebrhan, F. Miao and C. N. Lau, *Nano Lett.*, 2008, **8**, 902–7.
- M. Dvorak, W. Oswald and Z. Wu, *Sci. Rep.*, 2013, **3**, 2289.
- M. Terrones, *Nature*, 2009, **458**, 845–6.
- X. Li, X. Wang, L. Zhang, S. Lee and H. Dai, *Science*, 2008, **319**, 1229–32.
- Z. Zheng, C. Zhao, S. Lu, Y. Chen, Y. Li, H. Zhang and S. Wen, *Opt. Express*, 2012, **20**, 23201.
- Q. Bao, H. Zhang, B. Wang, Z. Ni, C. H. Y. X. Lim, Y. Wang, D. Y. Tang and K. P. Loh, *Nat. Photonics*, 2011, **5**, 411–415.
- X. Dong, Q. Long, J. Wang, M. B. Chan-Park, Y. Huang, W. Huang and P. Chen, *Nanoscale*, 2011, **3**, 5156–60.
- A. N. Abbas, G. Liu, B. Liu, L. Zhang, H. Liu, D. Ohlberg, W. Wu and C. Zhou, *ACS Nano*, 2014, **8**, 1538–46.
- B. Huang, Z. Li, Z. Liu, G. Zhou, S. Hao, J. Wu, B.-L. Gu and W. Duan, *J. Phys. Chem. C*, 2008, **112**, 13442–13446.
- E.-J. Kan, Z. Li, J. Yang and J. G. Hou, *J. Am. Chem. Soc.*, 2008, **130**, 4224–5.
- D. Boukvalov and M. Katsnelson, *Phys. Rev. B*, 2008, **78**, 085413.
- D. Wei, Y. Liu, H. Zhang, L. Huang, B. Wu, J. Chen and G. Yu, *J. Am. Chem. Soc.*, 2009, **131**, 11147–54.
- M. A. Rafiee, W. Lu, A. V Thomas, A. Zandiatashbar, J. Rafiee, J. M. Tour and N. A. Koratkar, *ACS Nano*, 2010, **4**, 7415–20.

- 16 T. Ando, K. Takayanagi, K. Kobayashi, Z. Chen, Y.-M. Lin, M. J. Rooks and P. Avouris, *Phys. E Low-dimensional Syst. Nanostructures*, 2007, **40**, 228–232.
- 17 J. Campos-Delgado, J. M. Romo-Herrera, X. Jia, D. A. Cullen, H. Muramatsu, Y. A. Kim, T. Hayashi, Z. Ren, D. J. Smith, Y. Okuno, T. Ohba, H. Kanoh, K. Kaneko, M. Endo, H. Terrones, M. S. Dresselhaus and M. Terrones, *Nano Lett.*, 2008, **8**, 2773–8.
- 18 L. Jiao, L. Zhang, X. Wang, G. Diankov and H. Dai, *Nature*, 2009, **458**, 877–80.
- 19 F. Li, E. Kan, R. Lu, C. Xiao, K. Deng and H. Su, *Nanoscale*, 2012, **4**, 1254–7.
- 20 D. V Kosynkin, A. L. Higginbotham, A. Sinitskii, J. R. Lomeda, A. Dimiev, B. K. Price and J. M. Tour, *Nature*, 2009, **458**, 872–6.
- 21 A. L. Elías, A. R. Botello-Méndez, D. Meneses-Rodríguez, V. Jehová González, D. Ramírez-González, L. Ci, E. Muñoz-Sandoval, P. M. Ajayan, H. Terrones and M. Terrones, *Nano Lett.*, 2010, **10**, 366–72.
- 22 S. Mohammadi, Z. Kolahdouz, S. Darbari, S. Mohajerzadeh and N. Masoumi, *Carbon N. Y.*, 2013, **52**, 451–463.
- 23 D. Wei, L. Xie, K. K. Lee, Z. Hu, S. Tan, W. Chen, C. H. Sow, K. Chen, Y. Liu and A. T. S. Wee, *Nat. Commun.*, 2013, **4**, 1374.
- 24 K. Kim, A. Sussman and A. Zettl, *ACS Nano*, 2010, **4**, 1362–6.
- 25 A. Morelos-Gómez, S. M. Vega-Díaz, V. J. González, F. Tristán-López, R. Cruz-Silva, K. Fujisawa, H. Muramatsu, T. Hayashi, X. Mi, Y. Shi, H. Sakamoto, F. Khoerunnisa, K. Kaneko, B. G. Sumpter, Y. A. Kim, V. Meunier, M. Endo, E. Muñoz-Sandoval and M. Terrones, *ACS Nano*, 2012, **6**, 2261–72.
- 26 A. G. Cano-Márquez, F. J. Rodríguez-Macias, J. Campos-Delgado, C. G. Espinosa-González, F. Tristán-López, D. Ramírez-González, D. A. Cullen, D. J. Smith, M. Terrones and Y. I. Vega-Cantú, *Nano Lett.*, 2009, **9**, 1527–33.
- 27 S. Ozden, P. A. S. Autreto, C. S. Tiwary, S. Khatiwada, L. Machado, D. S. Galvao, R. Vajtai, E. V Barrera and P. M. Ajayan, *Nano Lett.*, 2014, **14**, 4131–7.
- 28 F. Schwierz, *Nat. Nanotechnol.*, 2010, **5**, 487–496.
- 29 M. Zhang, S. Fang, A. a Zakhidov, S. B. Lee, A. E. Aliev, C. D. Williams, K. R. Atkinson and R. H. Baughman, *Science*, 2005, **309**, 1215–9.
- 30 A. E. Aliev, C. Guthy, M. Zhang, S. Fang, A. A. Zakhidov, J. E. Fischer and R. H. Baughman, *Carbon N. Y.*, 2007, **45**, 2880–2888.
- 31 and C. B. A. Brown, Matthew S., *Laser Precision Microfabrication*, Springer Berlin Heidelberg, Berlin, Heidelberg, 2010, vol. 135.
- 32 Z. H. Lim, A. Lee, Y. Zhu, K.-Y. Lim and C.-H. Sow, *Appl. Phys. Lett.*, 2009, **94**, 073106.
- 33 A. E. Aliev, M. H. Lima, E. M. Silverman and R. H. Baughman, *Nanotechnology*, 2010, **21**, 035709.
- 34 R. Brockmann, K. Dickmann, P. Geshev and K.-J. Matthes, *Int. J. Heat Mass Transf.*, 2003, **46**, 717–723.
- 35 E. Pop, D. Mann, Q. Wang, K. Goodson and H. Dai, *Nano Lett.*, 2006, **6**, 96–100.
- 36 A. E. Aliev, C. Guthy, M. Zhang, S. Fang, A. A. Zakhidov, J. E. Fischer and R. H. Baughman, *Carbon N. Y.*, 2007, **45**, 2880–2888.
- 37 P. Kim, L. Shi, A. Majumdar and P. McEuen, *Phys. Rev. Lett.*, 2001, **87**, 215502.
- 38 S. Jiang, C. Liu and S. Fan, *ACS Appl. Mater. Interfaces*, 2014, **6**, 3075–80.
- 39 D. K. Singh, P. K. Iyer and P. K. Giri, *J. Appl. Phys.*, 2010, **108**, 084313.
- 40 H. Matsuyama, M. Tachibana, T. Maki and M. Teramoto, *J. Appl. Polym. Sci.*, 2002, **86**, 3205–3209.
- 41 Z. Li, W. Zhang, Y. Luo, J. Yang and J. G. Hou, *J. Am. Chem. Soc.*, 2009, **131**, 6320–6321.
- 42 P. M. Ajayan and B. I. Yakobson, *Nature*, 2006, 441, 818–819.
- 43 L. Deng, R. J. Young, I. A. Kinloch, R. Sun, G. Zhang, L. Noé and M. Monthieux, *Appl. Phys. Lett.*, 2014, **104**, 051907.
- 44 D. Rossouw, M. Bugnet and G. Botton, *Phys. Rev. B*, 2013, **87**, 125403.
- 45 U. J. Kim, H. R. Gutiérrez, J. P. Kim and P. C. Eklund, *J. Phys. Chem. B*, 2005, **109**, 23358–65.
- 46 R. P. B. Dos Santos, E. Perim, P. A. S. Autreto, G. Brunetto and D. S. Galvão, *Nanotechnology*, 2012, **23**, 465702.
- 47 P. Castrucci, F. Tombolini, M. Scarselli, S. Bini, M. De Crescenzi, M. Diociaiuti, S. Casciardi, M. A. El Khakani and F. Rosei, *Phys. Rev. B - Condens. Matter Mater. Phys.*, 2007, **75**.
- 48 H. Kurata, E. Lefèvre, C. Colliex and R. Brydson, *Phys. Rev. B*, 1993, **47**, 13763–13768.
- 49 M. Acik and Y. J. Chabal, *Jpn. J. Appl. Phys.*, 2011, **50**, 070101.